ENHANCEMENT OF SEISMIC IMAGE QUALITY BY LEAST SQUARES REVERSE TIME MIGRATION CASE STUDY ALBERTINE GRABEN SOUTH WESTERN UGANDA

MUKIIBI SSEWANNYAGA IVAN[1], JIAN-PING HUANG[2], XINRU MU[3] and JIDONG YANG[4]

[1] Geosciences Department, China University of Petroleum (East China), Qingdao 266580, P.R. China. simukiibi267@gmail.com
[2] Pilot Laboratory for Marine Sciences and Technology, Qingdao 266000, P.R. China. Jphuang@upc.edu.cn
[3] Geosciences Department, China University of Petroleum (East China), Qingdao 266580, P.R. China. xinrumu@126.com
[4] Geosciences Department, China University of Petroleum (East China), Qingdao 266580, P.R. China. Jidong.yang@upc.edu.cn

(Received February 28, 2022; revised version accepted September 14, 2022)

ABSTRACT

Ivan, M.S., Huang, J.-P., Mu, X.R. and Yang, J.D., 2022. Enhancement of seismic image quality by least squares reverse time migration case study Albertine graben south western Uganda. *Journal of Seismic Exploration*, 31: 523-544.

Reverse Time Migration (RTM) is a conventional two-way wave-based method up to date known as the most popular imaging technique for complex subsurface structures. The technique uses the adjoint wave field to approximate the inverse component of the migration. The adjoint is a bit inaccurate which limits the resolution, image quality, balance of amplitudes of the final image. Least squares reverse time migration (LSRTM) is an iteration technique which can overcome the challenges faced by RTM as we incorporate the Least Square Inversion (LSI) algorithm into the RTM. Numerical tests were carried out on two models that is; multi-layer model (listric faults), positive flower structure model to validate the effectiveness of LSRTM technique in seismic imaging. Single trace comparison between the reference/true reflectivity to the RTM (LSRTM =1), LSRTM at the 10th and 30th iteration was analyzed for all the models. A clear strong positive correlation between true reflectivity and 30th iteration image was noted for all the two models in comparison with the RTM image. High convergence rates were noted after plotting the data residuals against iteration numbers. In all models a sharp decrease in the data residuals were noted before the 10th iteration followed by a gradual decline from 10th to 30th.

LSRTM can greatly suppress migration artefacts, acquisition noise and amplify the signal, balance the amplitude as portrayed on the single trace comparison diagrams for all models and enhance resolution (thinner reflection events) in comparison with RTM images. The algorithm is highly sensitive to low S/N ratio noise but good images are guaranteed at high S/N ratio above 10.0 dB.

KEY WORDS: migration, imaging, signal-to-noise ratio, inversion, Flower structure.

0963-0651/22/$5.00

INTRODUCTION

The Albertine graben is part of the Western branch of the East African Rift System (EARS) which stretches from Zambia (L. Malawi) and terminates on to the Central African Rift System (CARS) in South Sudan.

The Albertine graben stretches from South Sudan boarder (North) to L. Edward (South) total distance of 570 km and a width of 45 km (Dou et al., 2004). It was formed due to extension forces pulling apart leading to the down throw of the middle block forming the Albertine graben with bordering fault escarpment. Sedimentation then occurred in the basin under lacustrine, fluvial, beach and deltaic environments depositing gravel, sands, silts and clays under the different deposition environments (Kiconco, 2005). Stratigraphically the Albertine graben is subdivided into seven (7) major units from top to bottom, i.e., Rwebisengo Fm, Nyaburogo Fm, Nyakabingo Fm, Kasande Fm, Oluka Fm, Kakara Fm, Kisegi Fm and pockets of Karoo like formations (Pickford et al., 1994). The detailed positive flower structure model with the different formations is attached in the Appendix.

The EARS constitute of numerous positive flower (transpressional) structures which suggest that extensional tectonics followed by compressional/thrusting tectonic regimes (Kiconco, 2005) are responsible for the formation of these structures. positive flower structures mainly comprise a shallow antiform, upward spreading strands of reverse faults, and a few normal faults.

The intense tectonic activity affected the already gas saturated layers posing imaging problems in some parts of Albertine graben. Heritage Oil and Gas Company (2010) acquired seismic 2D lines and Tullow oil company acquired 3D seismic cube in the different parts of the fields in the graben. Data was processed using Post stack Time Migration method unfortunately the reflectors are poorly illuminated with low Signal to Noise ratio (S/N).

The LSRTM technique greatly improves imaging resolution by compensating for irregular illumination caused by acquisition geometry and complex Geological structures. The method also is very powerful at balancing seismic amplitude in imaging.

Reverse Time Migration (1st iteration of LSRTM) being a two-way wave migration technique tends to overcome almost all the challenges faced by the one-way wave migration-based techniques including accurate imaging of steeply dipping structures and increased resolution among complex geological structures. The drawbacks of RTM arise from the inaccurate inversion operator used, which distorts the final image in case of under-sampling, uneven subsurface illumination band-limited source wavelet and the limited recording aperture (Yang et al., 2019).

In case of thin layers with high velocity contrasts, the imaging result generated is highly distorted due to the strong low frequency noise generated. LSM is suitable for the attenuation of these artifacts as compared

to the post migration processing tools including application of the Laplacian filter which removes both the useful signal and the artifacts (Fan et al., 2016; Lei et al., 2018; Li et al., 2017; Mu et al., 2020).

LSRTM technique is a combination of both LSM and RTM, thus the technique combines all the advantages of both methods to give a more realistic, resolved and clearer subsurface image (Dai et al., 2012; Dong et al., 2012). The three steps for LSRTM includes; Reverse Time Demigration (RTDM), Reverse Time Migration (RTM) and searching direction estimation (Yongming and Qiancheng, 2019). RTDM based on Born approximation is used to generate the predicted data. We use the Conjugate Gradient Method (CGM), which is an iterative optimization algorithm, to estimate the search direction. Convergence speed was boosted by the use of the numerical line search approach known as the quasi-linear method and the step length determined.

Ongoing intensive seismic exploration activities call for precise seismic processing in the Albertine graben. The complex geological structures limit conventional RTM method to accurately image the subsurface. Therefore, by the use of LSRTM technique, accurate seismic interpretation of complex geological structures and thin beds will be delineated with a high degree of confidence probably more reserves will be discovered.

LITERATURE REVIEW/THEORY ABOUT LSTRM

Reverse Time Migration (RTM)

To date, RTM is the most effective imaging method for prestack depth migration of complex structures because it uses two-way wave equation for wavefield propagation and has no dip limitation (Chang and McMechan, 1987; Caldwell, 1999; Du et al., 2012; Yao, 2013; Nguyen and McMechan, 2015; Zhao et al., 2017; Fang et al., 2019). Conventional RTM is formulated as the adjoint operator of forward modeling rather than the inverse operator (Claerbout, 1992). With irregular acquisition geometry and limited wavelet frequency-band, the images derived from RTM might have unsatisfactory subsurface illumination and spatial resolution. Conventional RTM does not formulate the reversal procedure as an inverse problem. Instead of using a properly solved inverse operator, a conventional migration uses an adjoint operator of the wave propagation operator, for an efficient implementation. LSRTM provides a way to produce high-quality reflectivity images by iteratively approximating the inverse of the Hessian matrix.

Xue et al., 2011, modelled seismic data using the following equation

$$\boldsymbol{d}(x_r,\omega) = j\omega \iint \frac{2cos\theta}{v(x)} G_r(x_r,x,\omega) r(x,\theta) G_s(x,x_s,\omega) s(\omega) d\theta dx \quad , \qquad (1)$$

where $\boldsymbol{d}$ is the reflection data, θ is the angle of reflection, s is the source signature, $\boldsymbol{v}$ represents the velocity at the reflector, $G_s(x, x_s, \omega)$ is the green function from the source at position x_s to the reflector x, $G_r(x_r, x, \omega)$ is the green function from the reflector to the receiver x_r, $r(x, \theta)$ is the angle dependent on reflectivity and $\boldsymbol{j}$ is the imaginary unit. Since from the law of reflection of light angle of incidence is equal to the angle of reflection, then the dip factor $\frac{2cos\theta}{v(x)}$ is accurate for isotropic media.

Inversion of an angle independent/stacked reflectivity image simplifies [eq. (1)] yielding,

$$\boldsymbol{d}(x_r, \omega) = \int j\omega\, G_r(x_r, x, \omega)\boldsymbol{I}(x)G_s(x, x_s, \omega)s(\omega)dx \quad . \tag{2}$$

Conventional RTM, which applies an adjoint operator (Claerbout, 1992), can be expressed as

$$I(x) = \iint [j\omega G_r(x_r, x, \omega)\, G_s(x, x_s, \omega)s(x_s, \omega)]^{\dagger} d(x_s, x_r, \omega)dx_r d\omega \quad , \tag{3}$$

where † denotes the complex conjugate. The RTM which is based on eq. (2) can be implemented by the following steps: (1) convolving the product of the source and receiver Green's functions with the first-order derivative of the source wavelet $j\omega s(x_s, \omega)$, which generates a synthetic wavefield, (2) cross-correlating the synthetic wavefield with the recorded seismic data, (3) summing the overall traces, and (4) summing the overall frequencies. The last step is called the zero-lag image condition.

RTM gives correct positions and times but inaccurate amplitudes because the adjoint operator only deals with the kinematic information of the wavefield (Grohmann et al., 2015).

Least Square Migration (LSM) and least square inversion

Least squares migration is based on orthogonality that is the shortest distance from a point to a plane is carried by a line segment perpendicular to the plane (Sauer, 2012).

The basic theory framework of LSM was proposed by Tarantola (1984). LSM has been applied to the ray-based migration (Nemeth et al., 1999; Dai et al., 2012) and the one-way wave migration (Kühl and Sacchi, 2003; Clapp et al., 2005; Zhu et al., 2018). With the advancement of computational technology, LSRTM, which is based on the two-way wave equation, is implemented, and handles large scale synthetic and field data (Dai and Schuster, 2013; Zhang et al., 2015; Yang et al., 2016; Li et al., 2017a; Liu et al., 2017; Ping et al., 2017). Almost all geophysical problems are known to be non-linear though some can be linearized example Born approximation used to linearize migration (Yao, 2013). Consider a linear system of equation describing the migration problem [eq. (4)].

$$\mathrm{d}_{obs} = \boldsymbol{L}\mathrm{m} \quad . \tag{4}$$

The solution to the equation if solved in least square sense results into the Least Square Migration **(LSM).** The major purpose of the inversion is to find the earth's reflectivity matrix (m) by inverting the modelling operator **L**. In practice, the adjoint of the modelling operator is often used as an approximation to its inverse. Although approximate, it has some advantages including its tolerance to imperfections in the data and to certain extent allows incomplete data (Claerbout, 1992). The adjoint process can be expressed as

$$\mathrm{m} = \mathbf{L}^{\dagger}\mathrm{d}_{obs} \quad , \tag{5}$$

where † represents the conjugate transpose of **L**. Rarely the adjoint equates to the inverse thus it is necessary to implement the full inversion to achieve a more accurate result. It is worth noting that eq. (1) is not underdetermined, the unique generalized inverse of L can be found as a least-squares solution. The goal of least-squares inversion is to find a model that best describes the data, such that the objective function eq. (6) is a minimum. The major aim of LSM is to estimate a reflectivity model, such that the resultant waveform synthetics can best fit the observed data in the least-squares and single-scattering Born-approximation sense (Hao et al., 2016).

$$\varphi(\mathrm{m}) = ||\mathrm{d}_{obs} - \mathrm{Lm}||^2 \quad , \tag{6}$$

$$\text{at minimum } \frac{\partial\varphi(\mathrm{m})}{\partial(m)} = \frac{\partial[\mathrm{d}_{obs} - Lm]^{\dagger}[\mathrm{d}_{obs} - Lm]}{\partial m} = 0 \quad . \tag{7}$$

$$\mathrm{L}^{\dagger}Lm - L^{\dagger}d = 0 \quad . \tag{8}$$

Hence the Least square solution for eq. (1)

$$m = (L^{\dagger}L)^{-1}L^{\dagger}\mathrm{d}_{obs} \quad . \tag{9}$$

It can be noted that the solution to eq. (8) is unstable and eq. (9) also does not have a unique solution in cases where eq. (8) is an ill-posed system.

Imposing additional constraints (regularization), bias the solution to stabilize the inversion (Aster et al., 2005). Tikhonov regularization method is widely used in geophysical inversions and involves modifying the objective function [eq. (6)] to

$$\varphi(\mathrm{m}) = ||\mathrm{d}_{obs} - \mathrm{Lm}||^2 + \lambda^2||\mathrm{Tm}||^2 \quad , \tag{10}$$

where λ^2 is called the regularization parameter, and T is the Tikhonov regularization matrix. Minimizing the objective function given by eq. (7) is equivalent to solving

$$\begin{pmatrix} L \\ \lambda\mathrm{T} \end{pmatrix}^{\dagger}\begin{pmatrix} \mathrm{d}_{obs} \\ 0 \end{pmatrix} = \begin{pmatrix} L \\ \lambda\mathrm{T} \end{pmatrix}^{\dagger}\begin{pmatrix} L \\ \lambda\mathrm{T} \end{pmatrix}m \quad . \tag{11}$$

In this paper we did not use the regularization method. Inverting a large matrix needs massive computation and an explicit matrix formulation for seismic modelling is usually unavailable for LSM. Fortunately, iterative methods, such as conjugate-gradient method (CGM), Steepest-Descent Method (SDM) among others gradient techniques, overcome the above-mentioned problems. The CGM and SDM are the commonly methods because they eliminate the formation of an explicit matrix for modelling and approximate the solution more efficiently than other methods of inverting large matrices.

Steepest-Descent Method (SDM)

This is an optimization technique in which the solution is found by searching iteratively along the negative gradient direction which is the path of steepest descent of the objective function per iteration. This is achieved in two steps. Firstly, calculation of the direction of the steepest descent;

$$\mathrm{r(m)} = -\frac{\partial \varphi(\mathrm{m})}{\partial (m)} = \boldsymbol{L}^{\dagger}\mathrm{d}_{obs} - \boldsymbol{L}^{\dagger}\boldsymbol{L}\boldsymbol{m} \quad . \tag{12}$$

The second step is to determine the step length (α**)** by applying a line search along the steepest-descent direction. If the updated model m_1 reaches the minimal point in the steepest-descent direction, the derivative of the objective function with respect to the step length is zero, hence

$$\frac{\partial \varphi(\mathrm{m}_1)}{\partial (\alpha)} = \left[\frac{\partial \varphi(\mathrm{m}_1)}{\partial \mathrm{m}_1}\right]^{\dagger} \frac{\partial \mathrm{m}_1}{\partial (\alpha)} = 0 \quad . \tag{13}$$

Conjugate-Gradient Method (CGM)

Conjugate-gradient method is based on finding a linear combination of a set of search directions (vectors) to form the model error. The ideas behind conjugate gradients rely on the generalization of the usual idea of inner product (Sauer, 2012). Generally, for a linear system with n variables, the conjugate-gradient method converges in less than n iterations. Furthermore, the inversion continues to converge rapidly after the first few iterations, unlike the steepest-descent method, which converges slowly as the solution approaches the minimum. The Conjugate Gradient Method is a direct method that solves of the symmetric positive-definite system $\mathbf{Ax} = \mathbf{b}$ with the finite loop. In this paper the Conjugate-Gradient was employed.

The conjugate gradient iteration updates three different vectors on each step. The vector x_k is the approximate solution at step k. The vector r_k represents the approximate residual of vector x_k and d_k represents the new search direction used to update the approximation x_k to the improved version x_{k+1}.

The Conjugate Gradient finite loop

$$x_0 = initial\ guess$$
$$d_0 = r_0 = b - Ax_0$$
$$\text{for k} = 0,1,2,\ldots\ldots,\text{n} - 1$$
$$if\ r_k = 0,$$
$$stop,$$
$$end$$
$$\alpha_k = \frac{r_k^T r_k}{d_k^T A d_k}$$
$$x_{k+1} = x_k + \alpha_k d_k$$
$$r_{k+1} = r_k - \alpha_k A d_k$$
$$\beta_k = \frac{r_{k+1}^T r_{k+1}}{r_k^T r_k}$$
$$d_{k+1} = r_{k+1} + \beta_k d_k$$

End

Least Squares Reverse Time Migration

The combination of both LSM and RTM techniques resulted in the invention of the LSRTM. The method combines the advantages of the two-way wave equation for migration, and the accurate inverse operators of the LSM (Yao et al., 2015).

The least-squares RTM method attempts to minimize the difference between the observed field data and the synthetic data generated by the migration image. Hence, seismic migration should be posed as an inverse problem for finding an optimal reflectivity model through the following objective function (Lailly, 1984; Tarantola, 1984; Plessix and Mulder, 2004; Dai et al., 2012).

$$\emptyset_d\big(I(x)\big) = \|\mathrm{d}_{obs}(x_s, x_r, \omega) - d_0(x_s, x_r, \omega)\|_2^2 \quad , \qquad (14)$$

where $d_0(x_s, x_r, \omega)$ is the predicted data and $d(x_s, x_r, \omega)$ is the recorded data. RTM through this minimization is referred to as least-mean squares RTM.

This minimization can be achieved by using a variety of localized optimization methods. If only primary reflections are considered, which means the Green's functions are independent of reflectivity, differentiating [eq. (14)] with respect to $I(x)$ yields the gradient of the objective function as

$$\frac{\partial \varphi_d(I(x))}{\partial I(x)} = \sum_{\omega, x_r} Re\left\{[j\omega G_s s]^\dagger [G_r^\dagger(\mathrm{d}_{obs}(x_r, \omega) - d_0(x_r, \omega))]\right\} \quad , \quad (15)$$

where Re represents the real part of a complex number. Eq. (15) not only provides a means of calculating the gradient, but also gives it a physical meaning. In particular, $j\omega G_s s$ describes the forward-propagated wavefield from the first-order derivative of the source, while $G_r^{\dagger}(d_{obs}(x_r,\omega) - d_0(x_r,\omega))$ is the data residual, and $G_r^{\dagger}$ represents the backward propagation of the residual into the earth. The backward propagation is essentially equivalent to forward modeling the time-reversed residual as the virtual source.

The product of $G_r^{\dagger}\left(d_{obs}(x_r,\omega) - d_0(x_r,\omega)\right)$ with $j\omega G_s s$ followed by the summation equates to using the zero-lag cross-correlation imaging condition (Clearbout, 1971).

In the time domain eq. (15) yields:

$$\frac{\partial \varphi_d(I(x))}{\partial I(x)} = \sum_{I,x_r}\left[G_s * \frac{\partial s}{\partial t}\right][G_r \otimes (\mathrm{d}_{obs} - d_0)] \quad , \tag{16}$$

where $*$ and $\otimes$ are the convolution and cross-correlation operator, respectively. $\frac{\partial s}{\partial t}$ is the first order derivative of the source wavelet. Knowing the gradient and step length from the various gradient methods and secant method respectively, the reflectivity model can be updated iteratively [eq. (17)].

$$I_{n+1}(x) = I_n(x) + \propto q \quad , \tag{17}$$

where $\propto$ is the optimum step length per iteration and I represents the vector of the image and q is the vector of the update direction.

The inversion converges when the misfit is within an acceptable threshold ($\boldsymbol{\varepsilon}$) as shown in the workflow (Fig. 1) below.

NUMERICAL TESTS

The proposed method is tested on simulated 2D land data set. Two models are used to demonstrate the superiority of LSRTM in comparison with the RTM technologies in imaging complex geological structures in the subsurface. The synthetic seismic record is modeled using the acoustic 2D wave equation with constant density. The temporal derivative is discretized using the 2nd-order discretization scheme and the spatial mixed derivative is discretized using the 8th-order centered finite difference scheme in the following numerical examples. Perfectly Matched Layer (PML) absorbing conditions are used in our scheme and were implemented on four sides of

the model (Hu et al., 2007). The P-wave velocity models were constructed using Tesseral 2D software.

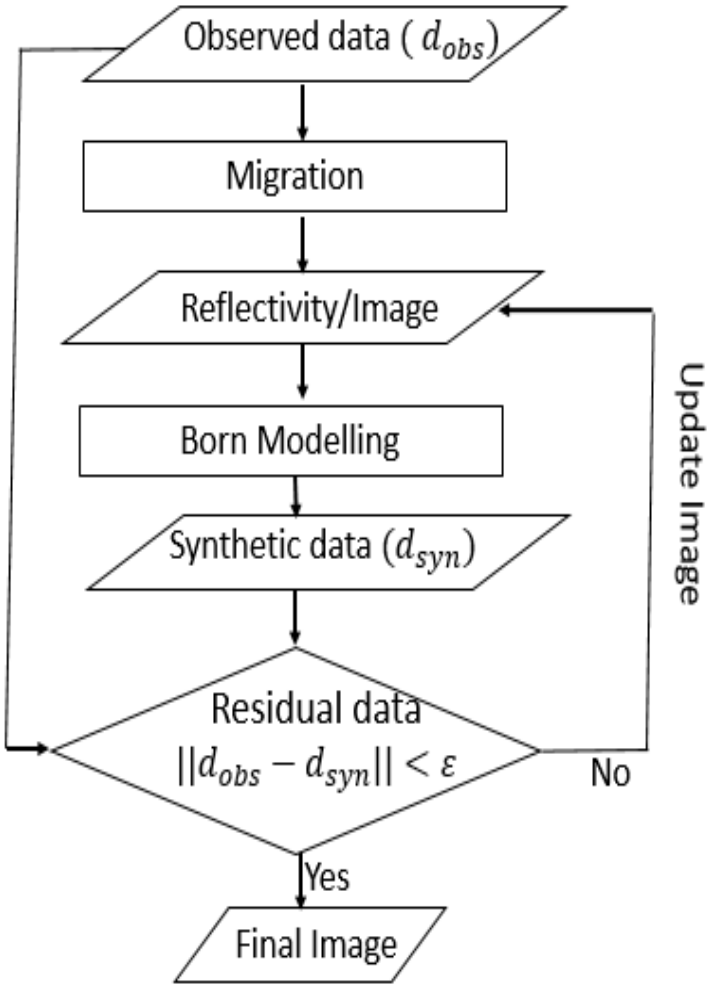

Fig. 1. LSRTM Workflow algorithm.

Multi layer horizontal model

Multi-layer model with alternating thin strata juxtaposed on to high angle normal faults and exhibiting strong velocity contrast is tested by the algorithm. This is a common phenomenon in some fields in the Albertine graben. Conventional imaging methods including RTM fail to delineate some of the thin layers exhibiting high velocity contrast (low resolution) yet these may be good reserviors for oil and gas. The model grid size for simulation is 401×201 grid points, grid spacing 10 m (horizontal and vertical).

Ricker source wavelet dorminant frequency of 20 Hz was used for synthetic generation at shot interval spacing of 40 m for 100 sources. The total number of geophones used for the simulation was 401 at a spacing of 10 m for the entire grid. The data was sampled at an interval of 1.0 ms for a record length of 2.0 s. LSRTM technique combines all good qualities of LSM and RTM, and it gave a better image after only 30 iteration as shown below in (Fig. 3d). Laplace filtering was used to remove the low-frequency noise in the imaging results. The final inverted image displays balanced amplitudes, enhanced SNR, and high resolution as compared to the 10th iteration image. Karoo formation (Appendix) a thin deepest anormously low velocity layer (Vp = 2200 m/s) is clear and continous in the final inverted image as compared to the RTM image. This is partly attributed to the high resolution and amplitude balancing property of the LSRTM algorithm, the improvements are indicated by red arrows (Fig. 3) at the same spot. The reflectivity comparision profile plots (Fig. 4) extracted at 1.0 km and 2.0 km shows that LSRTM closely approximates the true image and better fits the real data. By comparing Fig. 4a with Fig. 4b the events LSRTM events (red dotted box) approximate reference in comparison with RTM events due to the imbalance in amplitudes and noise.

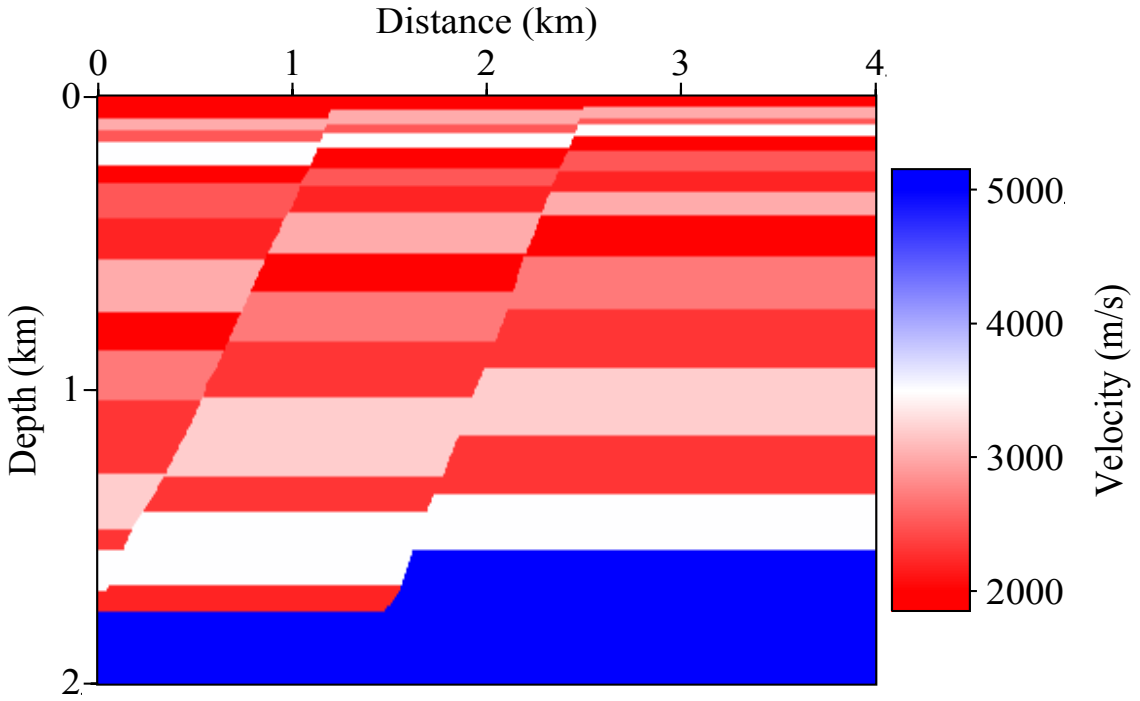

Fig. 2. True velocity model.

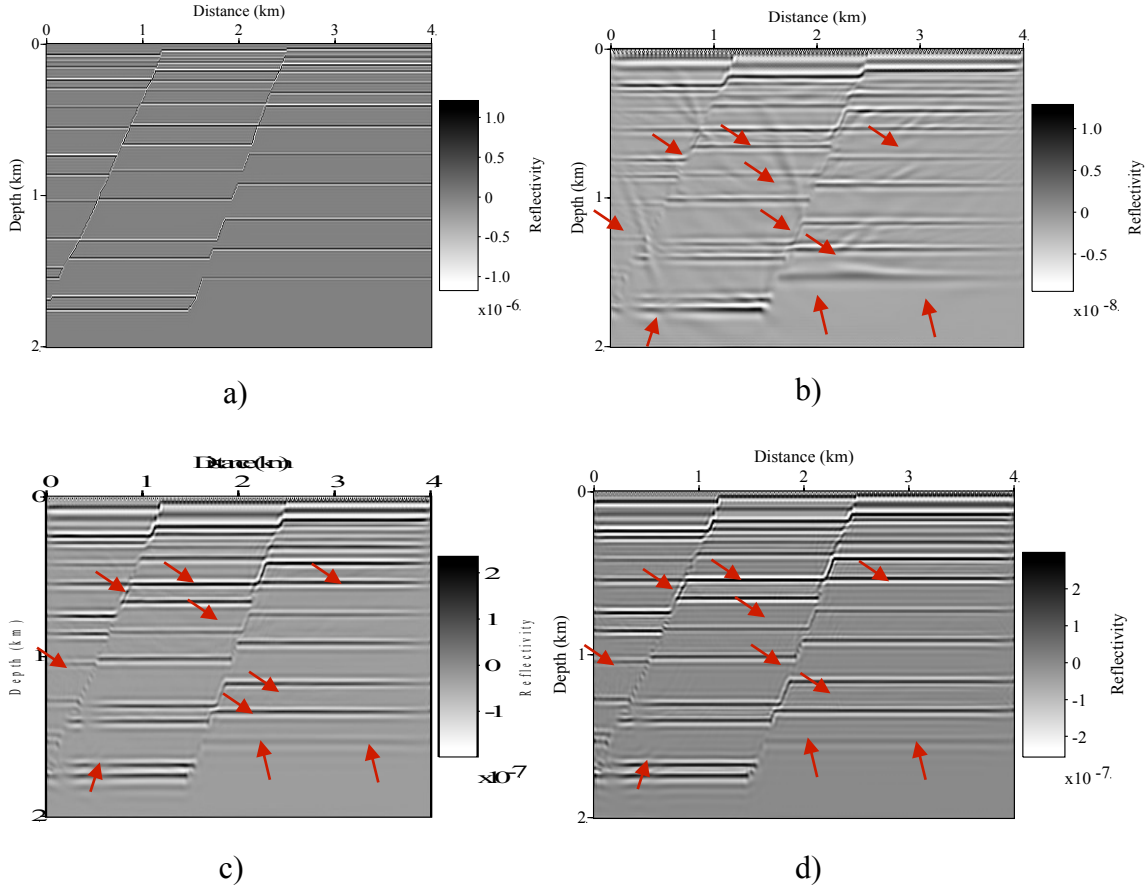

Fig. 3. Images of a) Reflectivity image, b) RTM, c) and d) LSRTM at 10th and 30th iteration respectively. LSRTM technique is a powerful technique in attenuating noise (Fig. 3d) increased SNR, neater faults, enhanced and balanced amplitudes in comparision to the RTM model (red dotted box). Notice the reflectivity of the final image is an order of magnitude compared to RTM result.

The unfiltered total wave number spectrum (Fig. 5) for the true image, RTM laplaced RTM, LSRTM at the 10th iteration and final inverted image was plotted. The final inverted image closely approximates the true image spectrum so does the 10th iteration image to the final image spectrum, and weak correlation is observed between RTM and true image. This is attributed to the strong low frequency noise in the RTM image. It can be concluded that LSRTM maintains the spectral component of each wave, recovered high frequency energy with increasing iteration despite the complexity of the model.

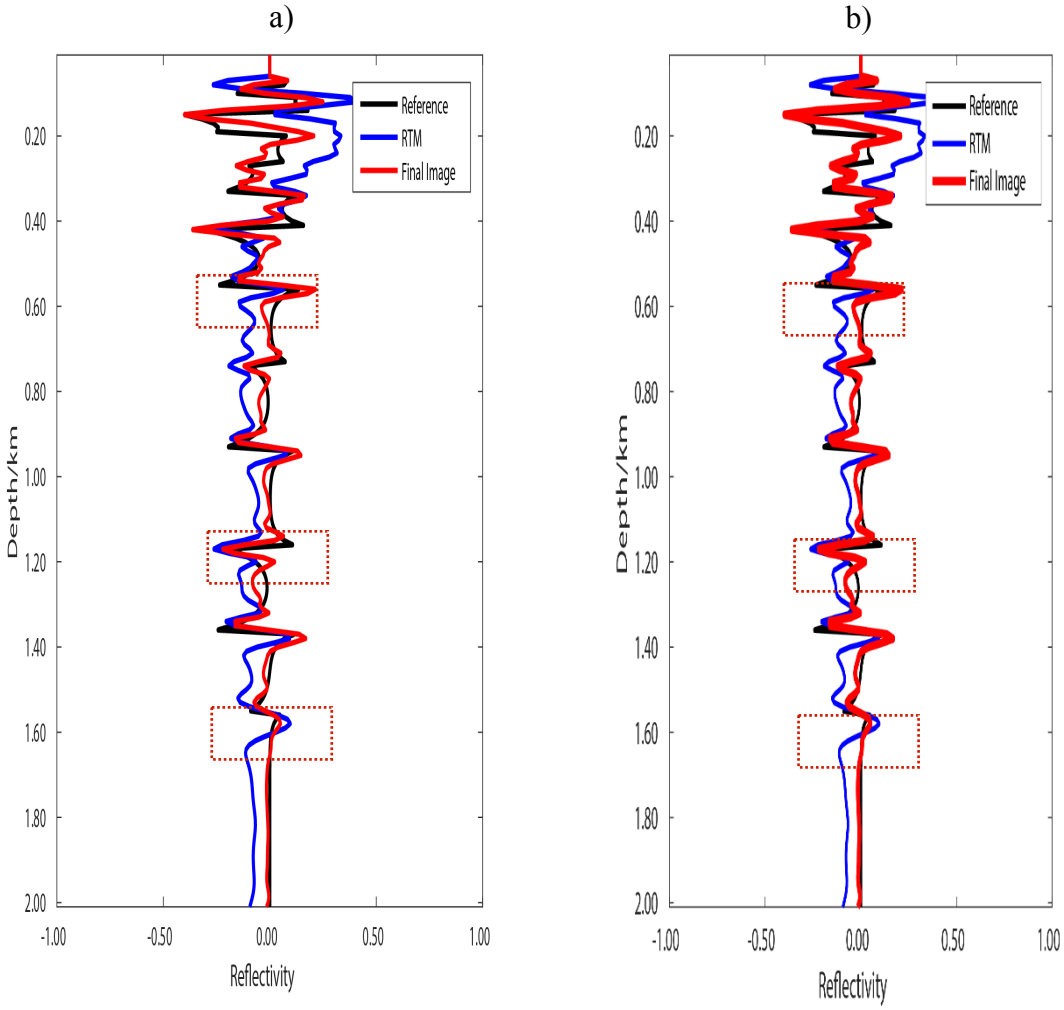

Fig. 4. Comparison between vertical reflectivity profiles extracted from reference, RTM and final image at a) 1.0 and b) 2.0 km, respectively. The inverted final image approximates the true image in phase and amplitude (red dotted rectangle).

The unfiltered total wave number spectrum (Fig. 5) for the true image, RTM laplaced RTM, LSRTM at the 10th iteration and final inverted image was plotted. The final inverted image closely approximates the true image spectrum so does the 10th iteration image to the final image spectrum, and weak correlation is observed between RTM and true image. This is attributed to the strong low frequency noise in the RTM image. It can be concluded that LSRTM maintains the spectral component of each wave, recovered high frequency energy with increasing iteration despite the complexity of the model.

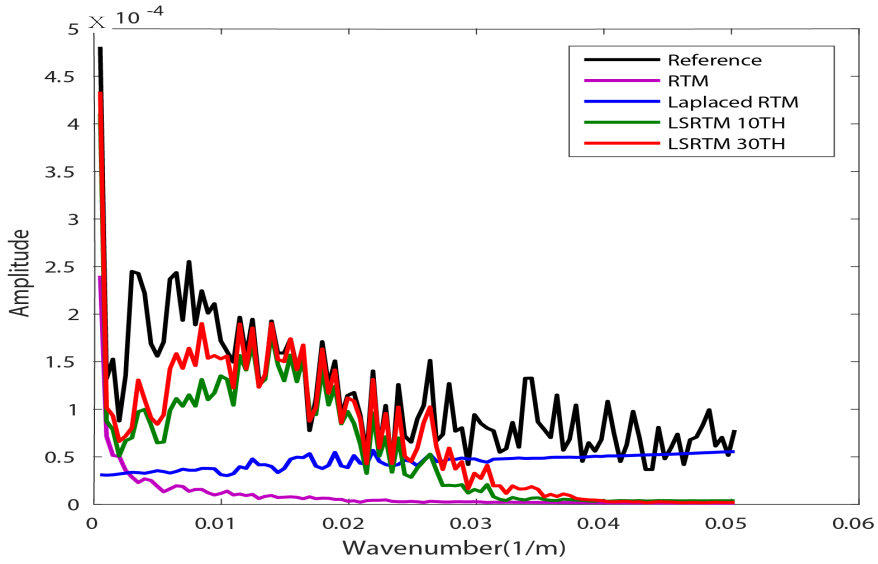

Fig. 5. Comparision amplitude spectrums for unfiltered RTM, Laplace filtered RTM final image at the 10th and 30th iteration and true image. The final image spectrum closely approximates the true image.

Positive flower structure model

The LSRTM algorithm is tested on positive flower structure typical in rift basins, e.g., Ugandan's Albertine graben, model size to 601×301, grid interval of 10 m (Fig. 5a). The flower structure comprises of high angle faults, anomalously low velocity layers, steeply dipping beds among others incapable of being imaged accurately by conventional migration techniques. The acquisition system comprise a total of 601 geophones and 301 shot points evenly deployed on the surface with an interval of 10 m and 20 m respectively. A Ricker source wavelet with a peak frequency 25.0 Hz is used as the source wavelet signature. The data was sampled at an interval of 0.5ms for a record length of 2.50 s.

The reflectivity image, RTM and final inverted imaging result were Laplace filtered (Fig. 6). The following observations were noted; Firstly, the LSRTM image had fewer artifacts than the RTM image basically the low frequency (Fig. 6d). Despite the fact that LSRTM image is neater, traces of migration noise are visible red dashed arrows zoom view (Fig. 7b). Neglecting anisotropy is used to explain the migration artifacts, but the acoustic wave equation is used in both, modelling and the migration algorithms. Source acquisition noise present in shallow layers (dotted black square) are greatly minimized in the final inverted image and resolution is highly boosted. The artifacts in the RTM image are residuals in LSRTM, which progressively diminish in the subsequent iterations. As a result, the LSRTM generates neater image. Deeper nearly vertical faults and folded layers are more apparent in Fig. 6d as compared to 6c due to imbalanced amplitudes, low frequency noise and multiple reflection. The Karoo formation (Appendix) with anomalously low velocity, it's very clear and continuous on the final image.

A low-quality RTM image is observed in (Fig. 6c) especially in the deeper parts of the image, this is probably due to, shielding of thin low velocity strata by high velocity strata (strong acoustic impedance and velocity contrast) example the Karoo Fm beneath by Kisegi Fm, resulting in severe amplitude dissipation inhibiting imaging of the deeper sections due to weaker energy. A high quality LSRTM image is obtained after 30 iterations (Fig. 6d). This is attributed to;

Firstly, the balancing of the imaging amplitudes resulting in improvement in imaging resolution. The LSRTM image amplitudes are more accurate and balanced. For example, the deep reflectors in the final inverted image, as expected, have almost the same amplitude as the shallow reflectors.

Finally, the LSRTM algorithm uses the inverse operator and the deconvolution imaging condition (Yao et al., 2012a) iteratively which sharpens the source signature thus high quality in comparison with cross correlating imaging condition of RTM which amplifies the source signature imprints.

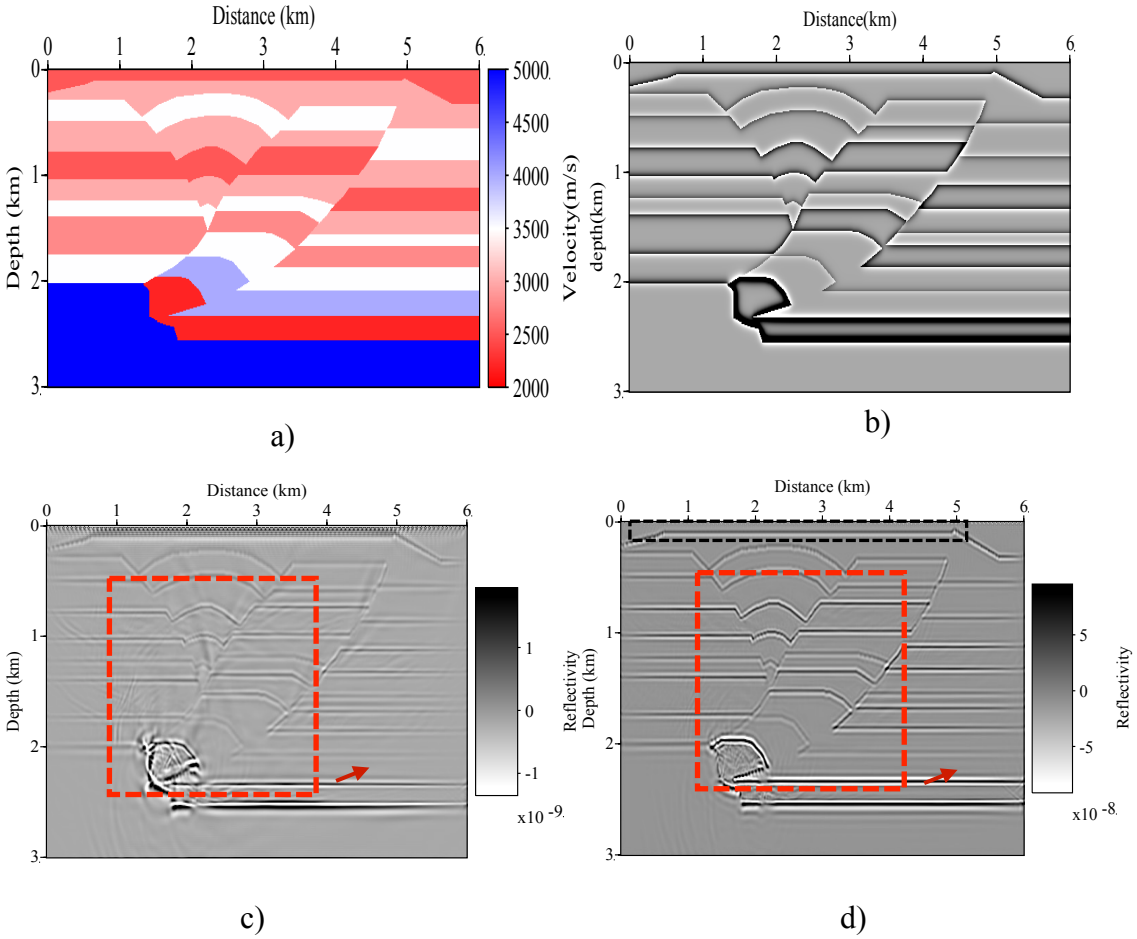

Fig. 6. Positive flower structure model: a) True Velocity model b) Reference reflectivity model, c) RTM image and d) inverted image after application of Laplacian filter. Red arrows depict resolution enhancement and amplitude balance in karoo strata. Supression of acquisition noise in Fig.6d (black dotted box) red square dotted box zoom view sections to compares the degree of image quality, black dotted box depicts enhancement in resolution (thin reflector event) in the final image.

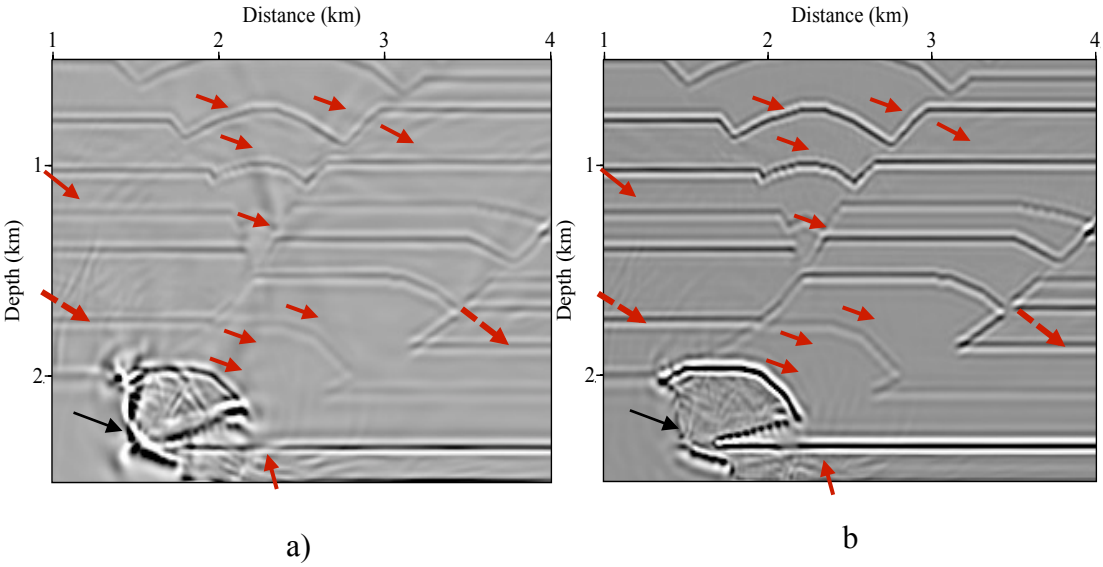

Fig. 7. Zoom view of the red boxed section in Fig. 6. a) RTM and b) LSRTM image showing an increase in resolution (SNR), clear visualization of high angle normal fault (black arrow) and attenuation of low frequency noise (red arrows) in the inverted image as compared to RTM image.

Single traces depth profile series of true reflectivity, RTM and final inverted image were extracted at 1.0 km (off the flower structure) and 3.0km (through the flower) were extracted (Figs. 8a and 8b), respectively. A perfect match in amplitude and phase between true reflectivity image and the final inverted image at shallower depth for both locations was noted. Noticeable deviations below 1.0 km depth are noted at both locations within the profile series. This is generally attributed to the relatively weaker illumination at depth. The deviations are relatively more severe at 3.0 km distance (Fig. 8b). Although the flower structure is more illuminated, but the complexity of geology within the structure results into noise and slight mismatch with the true reflectivity profile.

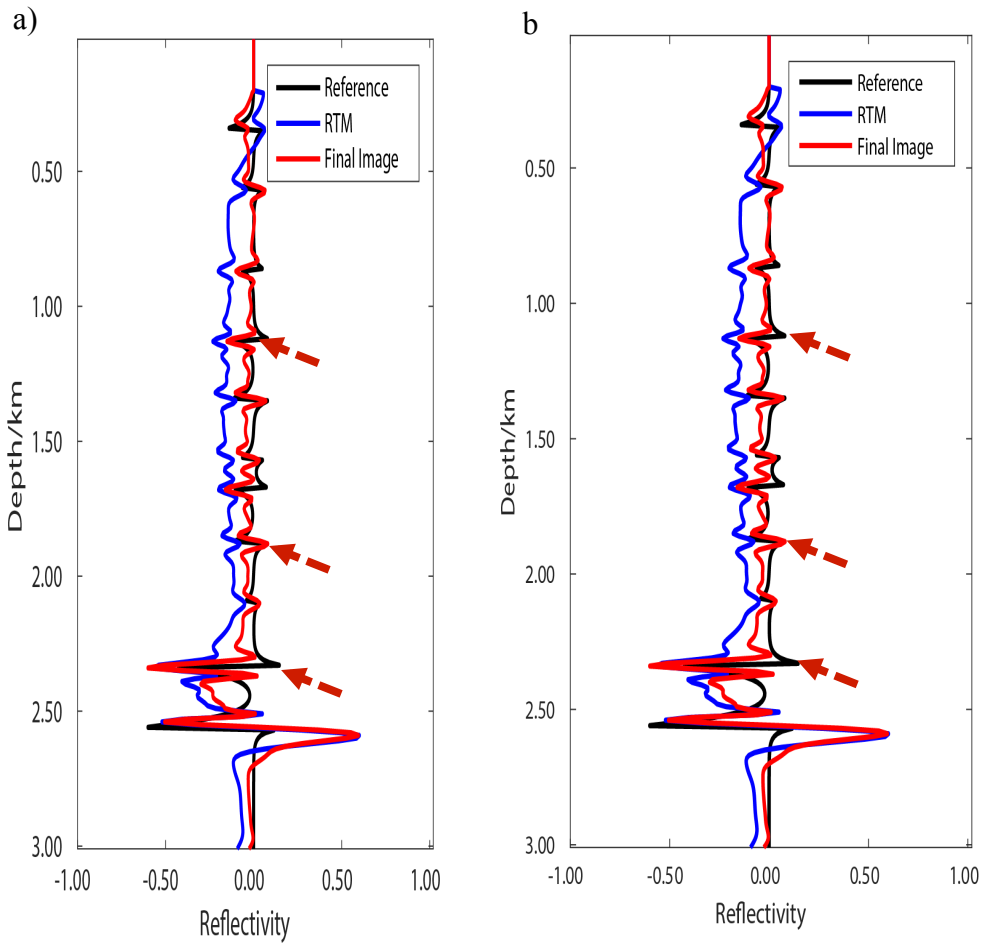

Fig. 8. Comparison between single trace reflectivity depth profiles extracted from the reference (black curve), RTM (blue line) and final image (red dotted line). The three-profile series are extracted a two locations, a) 1.0 km and b) 3.0 km. RTM curve is almost constant throughout the profile and final image reflectivity depth profile is in phase and approximates the amplitude of the true image.

The unfiltered total wave number spectrum for the true image, RTM, laplaced RTM, LSRTM at the 10th iteration and final inverted image (Fig.9) was obtained by calculating the wave number spectra of each trace in the vertical direction and adding the spectra of each trace in the horizontal direction. The final inverted image closely approximates the true image spectrum so does the 10th iteration image to the final image spectrum, and weak correlation is observed between RTM and true image. This is attributed to the strong low frequency noise in the RTM image. It can be concluded that LSRTM maintains the spectral component of each wave, recovered high frequency energy with increasing iteration. This portrays the potential of the LSRTM algorithm to improve on the imaging resolution.

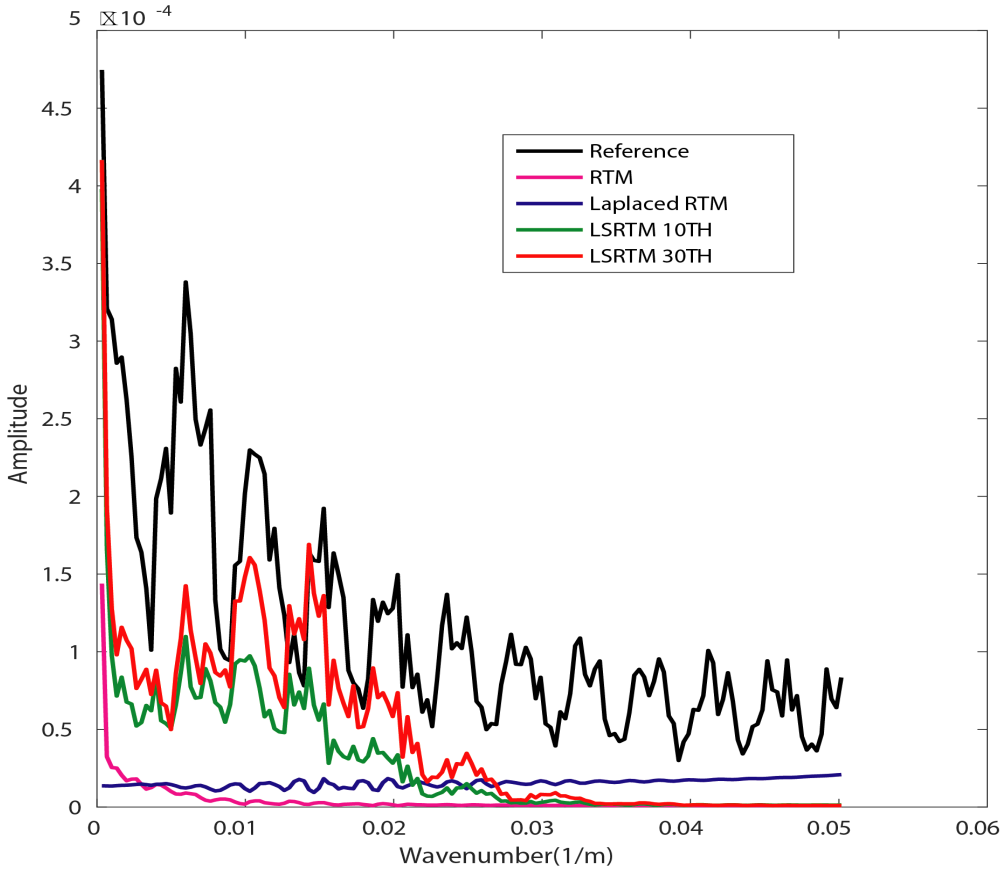

Fig. 9. Comparision amplitude spectrums for unfiltered RTM, Laplace filtered RTM final image at the 10th and 30th iteration and true image. The final image spectrum closely approximates the true image.

Sensitivity of LSRTM to Random Seismic Noise

Sensitivity of the LSRTM technique to random noise is analyzed. Pre-Stack Common Shot gather data was subjected to varying signal to noise ratio (S/N) of Gaussian probability distribution type. The LSRTM images obtained for different signal-to-noise ratios (SNR) after 30 iterations (Fig. 10) below. As it can be seen Fig. 10a, application of small amount of noise, the inverted image is a clear almost equivalent to LSRTM image without application of noise (Fig. 6d). Even deep layers and high angle fault imaging are visible. Noise intensity in imaging results increase with the decreasing S/N of the data. In (Figs. 10b and 10c), deep layers, zones of intense velocity contrast associated with weak reflected wave energy are the most severely affected, while shallow layers and inclined fault with strong reflected wave energy are accurately imaged. In case signal equates to noise (Fig. 10d) a blurred image and our flower structure is totally obliterated. Thin layers sandwiched within high velocity contrast layers (Karoo) and deeper regions are almost annihilated in the noise.

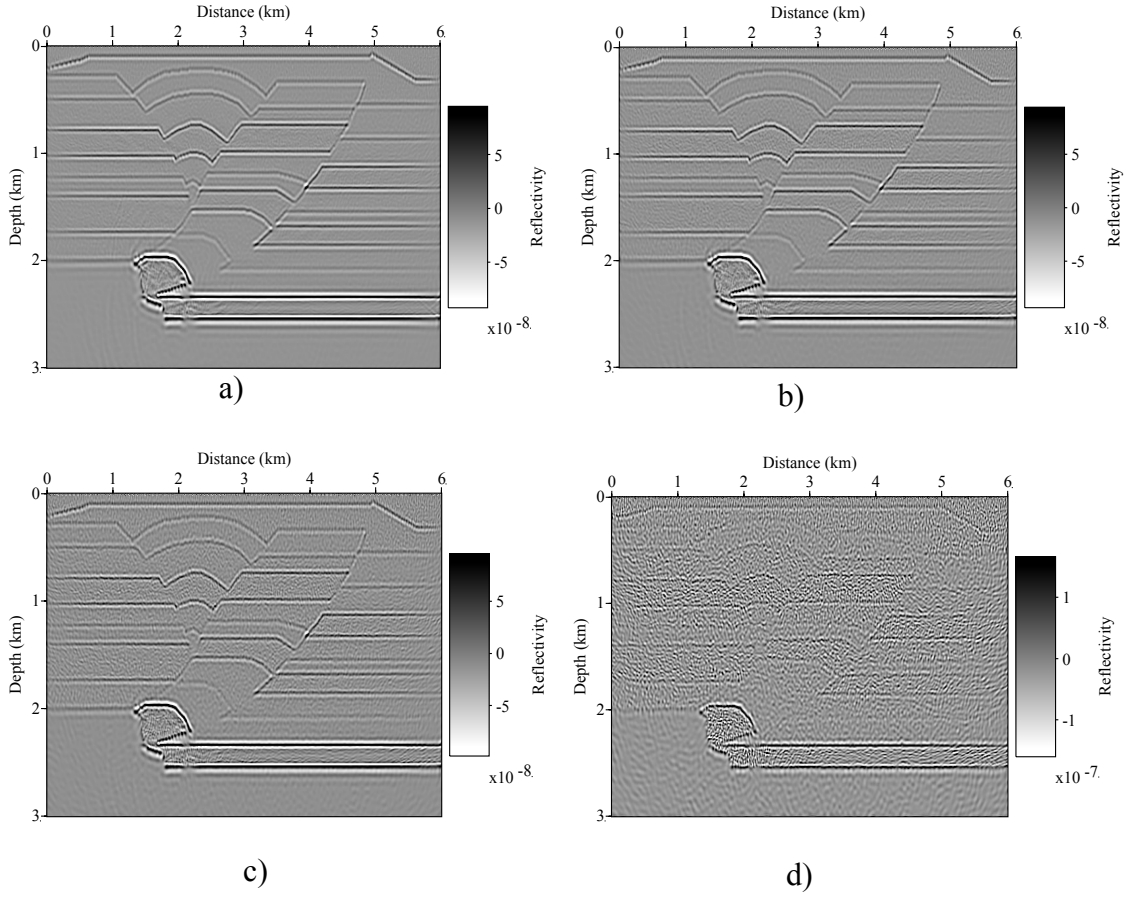

Fig. 10. Laplace filtered Final inverted Images from noisy shot data Gaussian noise. a) S/N = 20.0, b) 10.0, c) 5.0 and d) 1.0 dB.

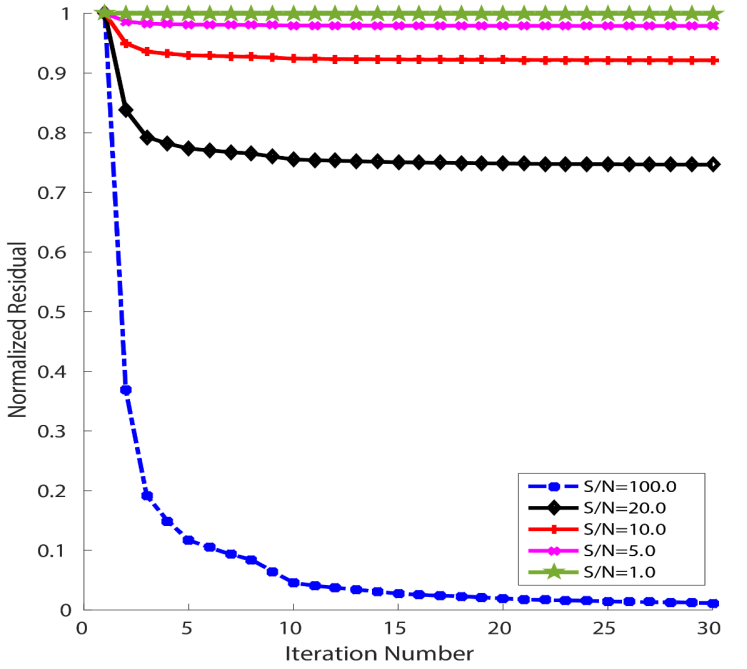

Fig. 11. Normalized data residual convergence curves of S/N = 100 dB, S/N = 20 dB, S/N = 10 dB, S/N = 5 dB, and SNR = 1.0 dB for the positive flower model.

Normalized data residual convergence curves for the observed data with different S/N ratios (S/N = 1.0, 5.0, 10.0, 20.0 and 100.0) are displayed (Fig. 11). It is very clear from the plot that for high S/N > 10.0 a high convergence rate at less than 5 iteration is noted. Constant plots (green curve) observed at S/N = 1.0 dB.

We extracted reflectivity depth logs at 3.0 km within the flower structure (Fig. 12). As can be seen with a low signal data, i.e, S/N = 1 the reflectivity plot is comprised of erroneous events as compared to the high S/N = 20 which is both in phase and closely approximates the reference profile (dotted red rectangle). Combining the imaging results, normalized residual plot and reflectivity depth profile it can be concluded that LSRTM algorithm is robust and converges at high S/N ratio above 10 dB.

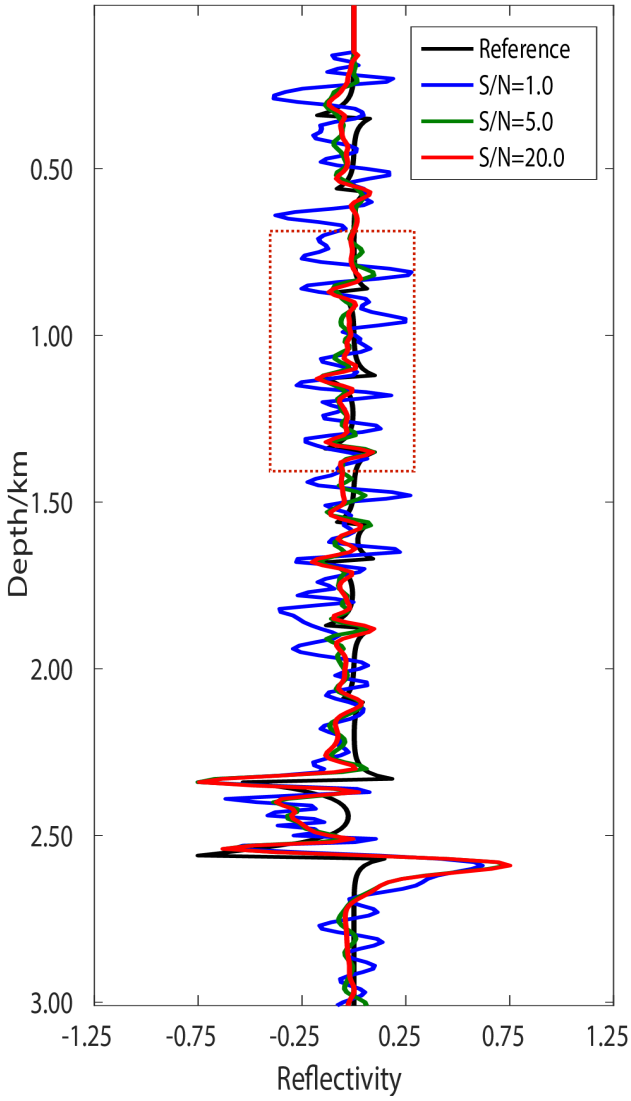

Fig. 12. Comparison between single trace reflectivity depth profiles extracted from the reference/ true (black curve), unfiltered LSRTM images (30th iteration) after applying Gaussian noise at S/N = 1.0, 5.0 and 20.0 dB midway 3.0 km. Our technique successfully attenuates noise for S/N > 10.0 thus closely approximates reference (red dotted rectangle) in shallower layers.

CONCLUSION

- The conventional constant density acoustic LSRTM technique greatly enhances imaging result in comparison with RTM (LSRTM @ 1st iteration) in all the two built velocity models as described in the numerical modeling section. RTM images are highly distorted by a low-frequency noise component, acquisition noise and LSRTM images were better resolved with better amplitude balance for successive iteration number.
- Balanced amplitudes and phase accuracy boost with increase in the iteration number this is very clear with the single trace comparison plots in all models (Iteration 30 the reflectivity curve approximates the reference curve).
- LSRTM technique is highly recommended for migrating data in geologically complex subsurface basins including the Albertine graben with a network of numerous transpressional/positive flower structures and micro stratum with a high velocity contrast.
- LSRTM techniques is highly sensitive to noise. From the numerical results it works best in limited noise acquisition setup. Thus, good imaging results are obtained at high signal noise ratio above 10.0dB.

REFERENCES

Aster, R.C., Borchers, B. and Thurber, C.H., 2005. Parameter estimation and Inverse Problems. Academic Press, New York.

Caldwell, J., 1999. Marine multicomponent seismology. The Leading Edge, 18: 1274-1282. doi: 10.1190/1.1438198

Chang, W.F. and McMechan, G.A., 1987. Elastic reverse-time migration. Geophysics, 52, 1365-1375. doi: 10.1190/1.1442249

Claerbout, J.F., 1992. Earth Soundings Analysis: Processing Versus Inversion. Blackwell Science, Boston.

Dai, W., Fowler, P. and Schuster, G.T., 2012. Multi-source least-squares reverse time migration. Geophys. Prosp., 60: 681-695.

Dong, S., Cai, J., Guo, M., Suh, S., Zhang, Z., Wang, B. and Li, Z., 2012. Least-squares reverse time migration: towards true amplitude imaging and improving the resolution. Expanded Abstr., 82nd Ann. Internat. SEG Mtg., Houston, 31: 1-5.

Dou, L., Wang, J., Cheng, D., Ran, X., Rubondo, E.N.T., Kasande, R., Byakagaba, A. and Mugisha, F., 2004. Geological conditions and petroleum exploration potential of the Albertine graben of Uganda. Acta Geologica Sinica ,78; 1002-1010.

Fan, J., Li, Z., Zhang, K., Zhang, M. and Liu, X., 2016. Multisource least-squares reverse-time migration with structure-oriented filtering. Appl. Geophys., 13: 491-499. doi: 10.1007/s11770-016-0580-y

Fang, J., Zhou, H., Chen, H., Wang, N., Wang, Y., Sun, P. and Zhang, J., 2019. Source-independent elastic least-squares reverse time migration. Geophysics, 84(1): S1-S16. doi: 10.1190/GEO2017-0847.1

Grohmann, M., Müller, S. and Niederleithinger, E., 2015. Reverse time migration: introduction of a new imaging technique for ultrasonic measurements in civil engineering. Internat. Symp., Non-Destructive Testing in Civil Engineering (NDT-CE), Berlin, Germany: 1-10.

Hao, H., Yike, L., Yingcai, Z., Xuejian L. and Huiyi, L., 2016. Least-squares Gaussian beam migration. Geophysics, 81(3): S87-S100. doi: 10.1190/geo2015 0238.1

Hu, W., Abubakar, A. and Habashy, T.M., 2007. Application of the nearly perfectly matched layer in acoustic wave modeling. Geophysics, 72(5): SM169–SM175. doi: 10.1190/1.2738553.

Kiconco, R., 2005. The Semliki Basin its Sedimentation History and Stratigraphy in Relation to Petroleum Accumulation. M.Sc. thesis, University of Capetown.

Kühl, H. and Sacchi, M.D., 2003. Least-squares wave-equation migration for AVP/AVA inversion. Geophysics, 68: 262-273. doi: 10.1190/1 .1543212.

Lei, Y., Trad, O.D. and Wenyong, P., 2018. Comparison between least-squares reverse time migration and full-waveform inversion. Geoconvention, Calgary, AB.

Li, C., Huang, J. P., Li, Z. C. and Wang, R.R., 2017b. Plane-wave least-squares reverse time migration with a preconditioned stochastic conjugate gradient method. Geophysics, 83(1): S33-S46. doi: 10.1190/geo2017-0339.1.

Mu, X., Huang, J. P., Yong, P., Huang, J. Q. and Guo X., 2020. Least-squares reverse time migration in TTI media using a pure qP-wave equation. Geophysics, 85(4): S199-S216. doi: 10.1190/GEO2019-0320.1

Nemeth, T., Wu, C.J. and Schuster, G.T., 1999. Least-squares migration of incomplete reflection data. Geophysics, 64: 208-221. doi: 10.1190/1 .1444517

Pickford, M., Senut, B. and Hadito, D., 1993. Geology and Paleobiology of the Albertine Rift Valley , Uganda-Zaire, CIFEG Publication Occassionale 1994/24, 179pp.

Ping, W., Shouting, H., and Ming, W., 2017. Least-squares RTM theory and application. 15th Internat. Congr., Brazil. Geophys. Soc.: 1-5.

Plessix, R.E. and Mulder, W.A., 2004. Frequency-domain finite-difference amplitude-preserving migration. Geophys. J. Internat., 157: 975-987.

Sauer, T., 2012. Numerical Analysis, 2nd Ed. Pearson Education Asia Ltd., ISBN 978-7-111-38582-0

Tarantola, A., 1984. Linearized inversion of seismic reflection data. Geophys. Prosp., 32: 998-1015.

Yang, J., Liu, Y., Yunyue, E., Li, E.Y., Cheng, A., Dong, L. and Du, Y., 2019. Joint least-squares reverse time migration of primary and prismatic waves. Geophysics, 84(1): S29-S40. doi: 10.1190/GEO2017-0850.1

Yao, G., 2013. Least Square Reverse-Time Migration. Ph.D. thesis, Imperial College, London.

Yao, G. and Wu, D., 2015. Least-squares reverse-time migration for reflectivity imaging. China Earth Sci., 58: 1982-1992. doi: 10.1007/s11430-015-5143-1

Yongming, L. and Qiancheng, L., 2019. A comparison of two reflectivity parametrizations in acoustic least-squares reverse time migration. Explor. Geophys., 51: 256-269. doi: 10.1080/08123985.2019.1682459

APPENDIX

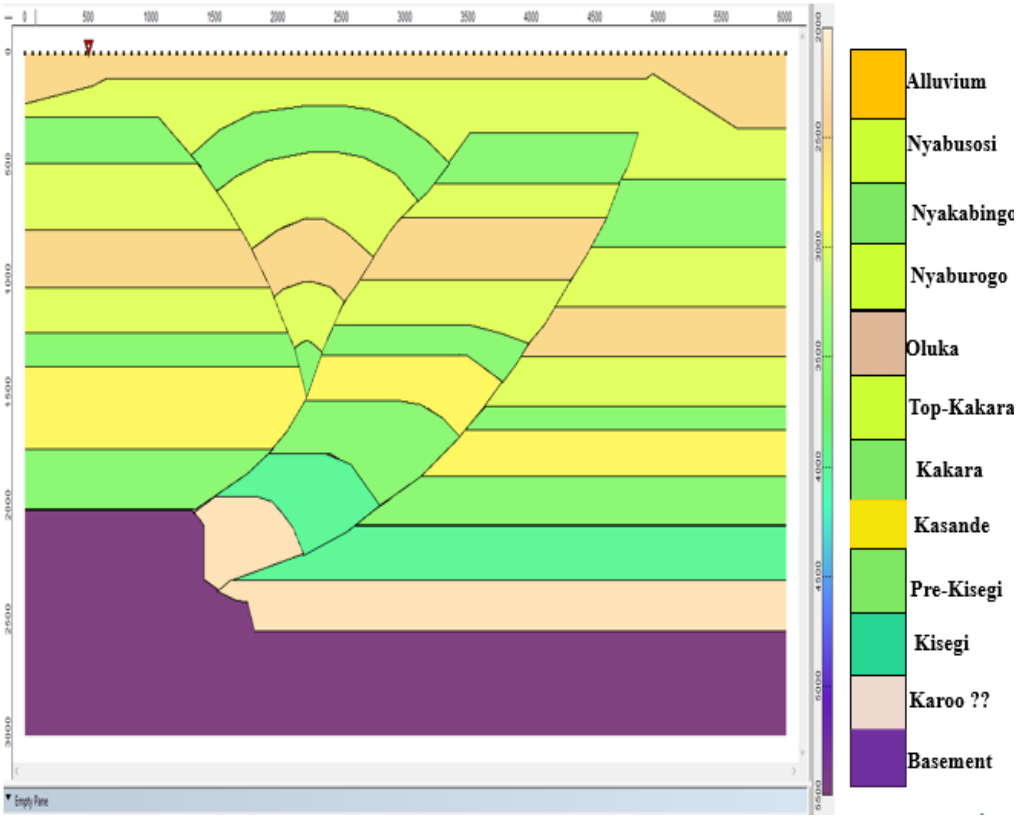

Fig. A-1. Stratigraphical model of the positive flower structure - Albertine graben.